INVESTIGATION OF A HELICOPTER MODEL ROTOR WAKE INTERACTING WITH A CYLINDRICAL SLING LOAD

Fabrizio De Gregorio, f.degregorio@cira.it, CIRA (Italy)
Antonio Visingardi, a.visingardi@cira.it, CIRA (Italy)
Ranieri E. Nargi, ranieriemanuele.nargi@gmail.com, University of Roma3 (Italy)

ABSTRACT

An experimental and numerical investigation on a four-blade isolated main rotor in hover condition has been carried out in order to investigate the effect of the rotor downwash on a tethered load. A sling load was located at different positions below the rotor disk in order to evaluate the mutual interference between the rotor wake and the immersed body. A radio controlled helicopter model, largely customized and modified for the scope of the experiment, was used as rotor rig. The sling load was reproduced by a low aspect ratio (l/d=2) cylinder being representative of typical loads as oil drums, water containers or engine canisters. Furthermore, the cylinder flow wake is a well known case largely investigated in literature and a good test case for computational fluid dynamics simulation. A six components balance measured the rotor loads calculating the figure of merit. The cylinder pressure distribution together with the flow field characteristics were also measured. Numerical simulation were carried out by using an unsteady, inviscid and incompressible free-wake vortex lattice boundary element methodology solver for multi-body configurations. The paper reports the main rotor wake characteristics up to 3 radii distance from the rotor plane with and without sling load. The effect of the downwash on the cylinder varying the distance and the changes induced by the presence of the cylinder are discussed.

1. NOMENCLATURE

Symbol	**Description**	**Units**
c	Chord length	m
CT	Helicopter rotor thrust coeff.	
FM	Figure of Merit	
Q	Rotor Torque	Nm
r	Local radius	m
r_c	Vortex core radius	m
R	Helicopter rotor radius	m
u, v, w	Velocity components	m/s
T	Rotor Thrust	N
V_θ	Swirl velocity	m/s
V_{Tip}	Velocity at blade tip	m/s
x, y, z	Geometrical coordinates	m
Γ	Vortex circulation	m^2/s
Δp	Pressure increment	N/m^2
θ_0	Collective, pitching angle	deg
σ	Helicopter rotor solidity	
Ψ	Blade azimuth position	deg
ω	Helicopter rotor speeds	RPM
ω_y	Out-of-plane vorticity component	1/s

2. INTRODUCTION

The ability to reach and hover above locations that no other vehicle can efficiently reach is a key aspect of helicopters. The capacity to operate immediately after natural disasters as earthquakes, tsunamis or floods and in case of interruptions of the land communication is of fundamental importance. In these cases, helicopters are the first aid to civil populations delivering goods, emergency staff, shelters, and rescuing people needing medical cares. These missions are accomplished by tethering an external load beneath the helicopter, giving rise to the term slung load or sling load operations. The helicopter sling loads have usually bluff body geometries characterized by complex three-dimensional unsteady aerodynamic phenomena. The addition of these tethered loads requires that each different load configuration be separately flight-tested for safety, as they can become unstable at higher flight speeds within the mission envelope (Gabel and Wilson[1]). The unavoidable consequence is that the presence of the sling loads reduces the helicopter forward speed thus resulting in slower rescue operations and fewer deliveries. The external loads carried by the helicopters are typically connected in the proximity to the fuselage in order to shadowing the main rotor loads and avoiding possible instability phenomena (Rajagopalan[2]). Instead, for some particular missions, such as search and rescue operations (SAR) or glide flight drop tests, the sling loads can be located at a larger distance from the fuselage. In these cases the knowledge of the rotor wake downwash effects and the forces and moments acting on the tethered loads becomes crucial not only for the safety of the mission but also when a controlled attitude of the load is required, Figure 1.

Figure 1: ESA-IXV (left) and Dream Chaser (right) space vehicles drop test.

The latter case is represented by the drop test of reusable launch vehicle (RLV) to simulate the final low-speed approach and landing phase of the re-entry from space. In 1998, the Boeing vehicle designed as X40-A carried out the first flight. The vehicle was dropped at 2740 m from a cradle below a UH-60 helicopter, and successfully flew to an automatic landing on a designated runway (Parsch[3]). In 2001, after that US Air Force joined the NASA X37 program, the same X40-A vehicle, performed several free flights from an altitude of 4500m dropped by a CH-47D. The German RLV, named PHOENIX, performed three glide flights from an altitude of 2400m in 2004 (Janovsky and Behr[4]), followed in 2013 by the European Intermediate Experimental Vehicle (ESA-IXV), released by CH-47C helicopter from an altitude of 3000 m (Rufolo et al[5]), and the glide test performed by Sierra Nevada Corporation Dream Chaser mock up on November 2017 (Foust[6]). In these cases, the carrier helicopter releases the space vehicle from a specific altitude in order to verify the manoeuvrability and to validate the autonomous guidance and navigation systems. The starting drop test condition can be crucial for the correct fulfilment of the mission that can be directly influenced by the rotor wake downwash. During the ESA-IXV test activities, it was clear that quite few information was available in literature regarding the rotor wake downwash at medium-to-large distances from the rotor disk, and the aerodynamic induced loads on the tethered test article.

This lack of information drives the interest of the present research activity that is aimed at investigating the rotor wake behaviour up to a distance of 3 rotor radii (R) from the rotor disk in hover conditions, and evaluates the induced loads on a sling loads immersed in the rotor wake. This research was carried out in the framework of the GARTEUR (Group for Aeronautical Research and Technology in Europe) Action Group 22 aimed at investigating “Forces on Obstacles in Rotor Wake” that saw the involvement of several research institutes and universities in Europe (Visingardi et al.[7]).

The present paper illustrates the experimental and numerical activities carried out to evaluate the effect of the main rotor downwash on a sling load located at different positions beneath the rotor plane. The first part of the paper describes the main characteristics of the four-bladed rotor rig, the sling load model, the experimental set-up and the numerical methodology applied. The rotor rig characterization, including the evaluation of the aerodynamic loads, the rotor downwash investigation, with and without sling load, and the blade tip vortex detections are then described. The final part of the paper illustrates the experimental results related to the dissipation of the tip vortex vorticity and to the static pressure distributions induced by the rotor wake to the sling load surface.

3. EXPERIMENTAL SET UP

3.1 Rotor Rig

A dedicated rotor test rig was developed based on an existing commercial radio controlled helicopter model (Blade 450 3D RTF), but largely customized and modified for the scope of the experiment, Figure 2. A four-bladed rotor with collective and cyclic control replaced the original two-bladed rotor hub. A new model frame was re-designed and built in order to withstand the rotor loads and vibrations once connected to the six components load cell. The tail boom and the tail rotor were removed in order to investigate the isolated main rotor only. The rotor presented four untwisted, rectangular blades with radius of R=0.36 m, root cut-out at 16% of the radius, chord length of c=0.0327m and a NACA0013 airfoil throughout the blade span, Figure 3. The resulting rotor solidity value was equal to σ=0.116. The clockwise rotor maximum speed was ω=1780 rpm, and the collective pitch angle θ_0 varied from 1 to 11.3 degree.

The rotor rig was mounted on a six components balance (ATI MINI40). The detailed characteristics in terms of full scale and accuracy are summarized in Table 1.

The rotor test rig was located at a distance of 5 R from the floor and 3 R from the ceiling to avoid any influence of the surrounding walls. One hale sensor was located on the shaft gear for measuring the rotating speed and providing a trigger TTL signal at prefixed azimuth angle in order to allow phase locking measurements.

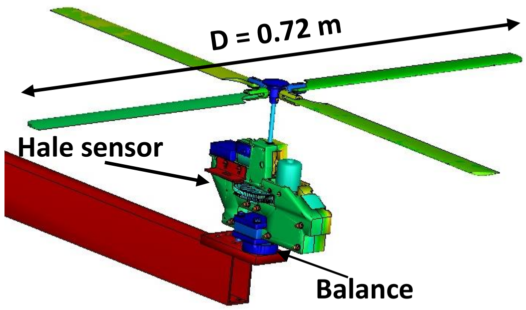

Figure 2: Rotor test rig

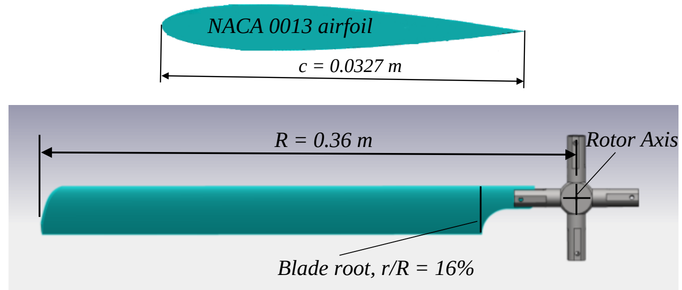

Figure 3: Airfoil (top) and planform (bottom) of the rotor blades, different scales in both sketches.

	Fx [N]	Fy [N]	Fz [N]	Mx [Nm]	My [Nm]	Mz [Nm]
Full scale	±20	±20	±60	±1	±1	±1
Accuracy	0.25	0.25	0.60	0.0125	0.0125	0.0125

Table 1: Balance characteristics

3.2 Sling Load

A 3D circular cylinder having aspect ratio of l/d = 2 (cylinder length and diameter of l=0.2m and d=0.1m respectively) was selected as representative of a typical sling load, such as the oil drums or the engine canisters described in Gabel and Wilson[1] and Prosser and Smith[8].

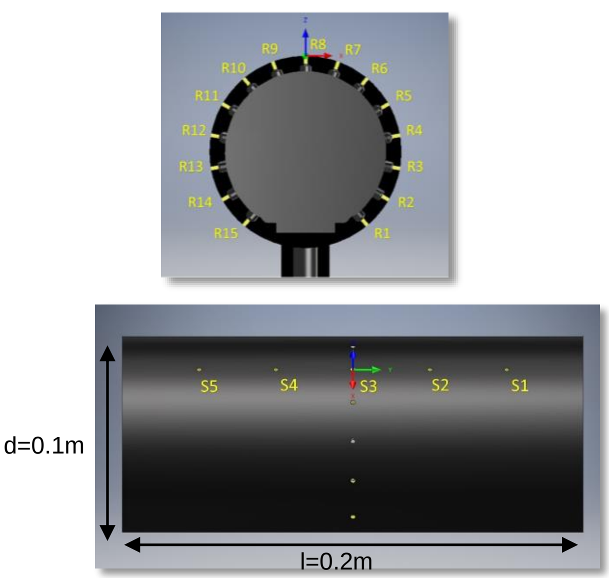

Figure 4: PTS locations on the cylinder: radial distribution (left); spanwise distribution (right)

Furthermore, the cylinder wake is well discussed in literature (Zdravkovich[9]) and the simple geometry was a good test case for the numeric simulation (Catalano et al.[10]). The cylinder was built by using an additive layer material 3D printer. The cylinder was equipped with 19 pressure taps: 15 azimuthally equally spaced ($\Delta\varphi$=20°) on the symmetry plane and 5 spanwise distributed on the top surface in order to monitor the surface pressure distribution, Figure 4.

The cylinder was able to house a multi-port ZOC33/64 pressure transducer module characterized by a full scale value of 10 water inches, corresponding to 2488 Pa, and measurement accuracy of 0.2% of the full scale. The cylinder was mounted on a movable support in order to investigate the effect of the downwash at different distances from the rotor disk plane.

3.3 PIV measurement system

The rotor downwash characteristics were measured by a standard two components measurement system composed by a double head Nd-Yag laser with a maximum energy of 320 mJ per pulse at 532 nm and a single double frame CCD camera (2048 by 2048 px) with a 50 mm focal length. The camera was mounted on a two components linear translating system in order to cover the full region of interest. The light sheet was vertically oriented and aligned with the rotor blade at the azimuth angle of Ψ=210°. The laser optics were also movable along the vertical direction in order to cover the full wake downwash. Particle images had an approximate diameter of ~2 pixels avoiding pixel locking problematics. As tracer particles, aerosolized di–ethylhexyl–sebacate oil droplets were injected into the region of interest.

Ten PIV measurement regions with size of 320 by 320 mm^2, partially overlapped, were used to measure the wake characteristics in an area of about 1 m^2, Figure 5. A better spatial resolution was chosen in order to track the blade tip vortices in the proximity to the rotor disk, these measurement were performed using a 200 mm focal length obtaining a measurement size of 120 x 120 mm^2. The optical resolution was about 6 px/mm and 17 px/mm for the downwash and tip vortex measurements, respectively. The time delay between the laser double–pulses was 35 μs and 25 μs for the smaller and larger optical resolution.

The images were preprocessed by applying a background grey-level subtraction. PIV-View 3.60 from PIVTEC was employed to process the images. The analysis consisted in a Multi-grid scheme with a B-Spline of 3rd order image deformation ending at 32x32 px^2 and 50% overlap. Correlation maps were calculated by FFT multiple correlation (Hart[11]) of 2 windows and a 3-point Gaussian peak fit was used to obtain the displacement. The results presented a velocity spatial resolution of Δx=2.7 mm and Δx=0.93 mm for the downwash and tip vortex measurements, respectively. The random noise of the PIV cross–correlation procedure can be estimated as 0.1 px as a rule–of–thumb (Raffel et al.[12]). Using the current values for the optical resolution (6.0 px/mm and 17 px/mm) and the laser double–pulse delay (35 μs and 25 μs), this related to a velocity error of ΔV of ~ 0.47 m/s and 0.23 m/s for the downwash and the tip vortex, respectively.

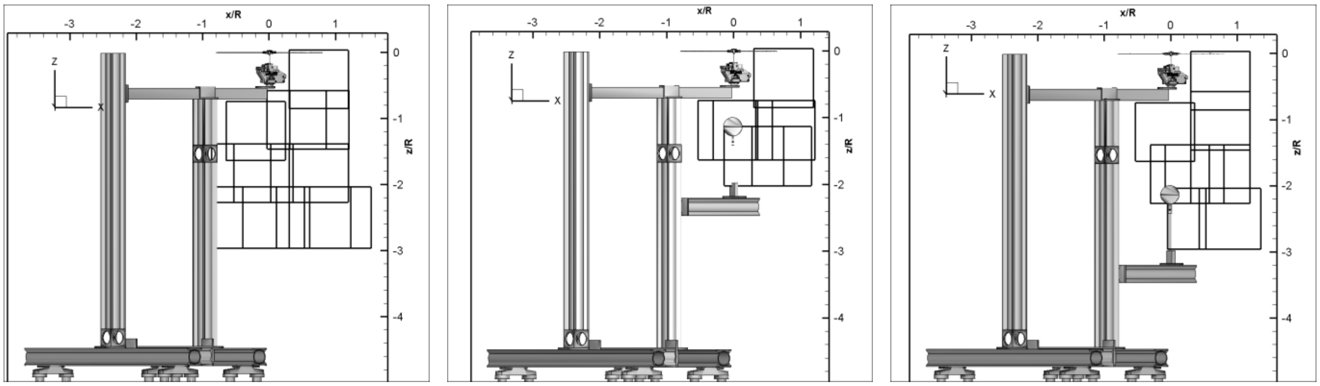

Nominal Hover

Cylinder at z= 1 R

Cylinder at z= 2 R

Figure 5: PIV measurement regions for the different test conditions: rotor in isolation; cylinder in the rotor downwash at z= 1 R, z=2 R and z=2.5 R, respectively.

The PIV space resolution is characterized by the measurement volume length Δx, and previous works (Martin et al.[13]) have shown that the correct measurement of the vortex characteristics is obtained for $\Delta x / r_c \leq 0.2$, where r_c is the vortex core radius defined as the distance from the vortex centre to the radial position where the maximum tangential velocity is reached, Figure 6. For this work, the tip vortex core radius was between 3mm to 3.3mm so the ratio $\Delta x / r_c$ was of about 0.31-0.28 comparable with the required value.

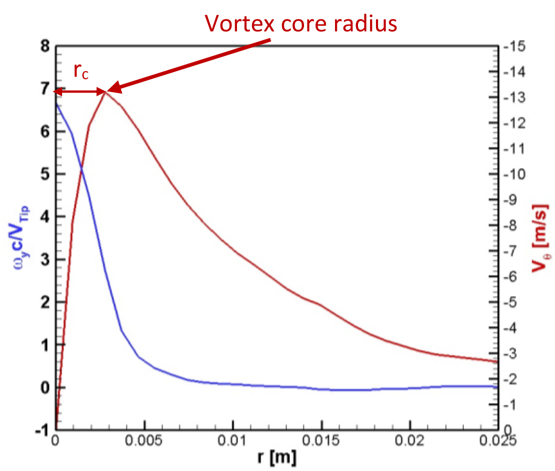

Figure 6: Tip vortex main characteristics. Tangential velocity and normalised out of plane vorticity vs vortex radius. The vortex core radius is detected by the maximum of tangential velocity (V_θ).

4. NUMERICAL METHODOLOGY

4.1 BEM methodology

The numerical computations have been carried out by using the code RAMSYS[14], which is an unsteady, inviscid and incompressible free-wake vortex lattice boundary element methodology (BEM) solver for multi-body configurations developed at CIRA. It is based on Morino's boundary integral formulation for the solution of Laplace's equation for the velocity potential φ. The surface pressure distributions are evaluated by applying the unsteady version of Bernoulli equation, which is then integrated to provide the forces and moments on the helicopter configuration and the surrounding obstacles.

In order to account for the viscous diffusion of the wake vortex elements, the Vatistas vortex core model has been used, according to which the swirl velocity is expressed as:

$$(1) \quad V_\theta = \frac{r\Gamma}{2\pi(r^{2n} + r_c^{2n})^{1/n}}$$

where the coeffcient n has been set to “1”, as suggested by Scully[15].

The applied diffusion model is the one described by Squire[16]. In this model the growth with time of the core radius r_c is given by:

(2) $r_c(t) = \sqrt{r_{c0}^2 + 4\alpha\delta\nu t}$

(3) $\delta = 1 + a_1 \frac{\Gamma_\nu}{\nu}$

The term r_{c0} is the initial core radius that removes the singularity at t_0, and has been set equal to a 3% of the blade average chord length c in the present computations. The constant term α is equal to 1.25643, while the product $\delta\nu$ represents the "eddy viscosity" and ν is the kinematic viscosity. Γ_ν is the circulation strength of the vortex element and the coefficient a_1 is an empirical parameter specified to vary between 0.2 and 0.0002, as indicated in Baghwat[17]. For a small-scale rotor, as the one used for these investigations, a value of 0.0002 can used.

No model for vortical dissipation, which accounts for the decay of the vortex element strength Γ_ν, has been applied.

4.2 Test set-up

Each of the four rotor blades has been discretised by 40 chordwise x 16 spanswise panels, with more panels concentrated towards the blade tip in order to produce a stronger tip vortex roll-up. An azimuth step $\Delta\psi = 10°$ has been selected for the time discretization.Twenty wake spirals have been used to model the wake, and twenty rotor revolutions have been considered in order to obtain a full convegence of the thrust coefficient. The fuselage has been modelled as a cuboid having the same main dimensions as the fuselage model and has been discretized by 488 panels. The cylinder has been discretized by 1120 panels,Figure 7. The computations have been performed at the same experimental thrust coefficient, equal to 0.00609, which has been obtained with a collective pitch $\theta_0 = 8.1°$.

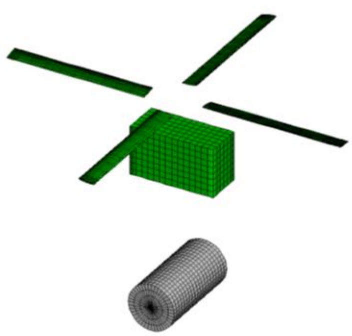

Figure 7: Geometry panel discretization

5. TEST MATRIX

The wake downwash generated by the four-bladed rotor was investigated both in isolation, without the presence of sling loads, and with the presence of a sling load located at different positions from the rotor disk (1 R, 2 R and 2.5 R). The investigation evaluated:

- The experimental rotor figure of merit FM at different rotor speeds and collective pitch angles;
- The characteristics of the wake downwash by PIV measurements and numerical simulations, with and without the presence of the cylinder;The experimental and numerical investigation of the blade tip vortex path and main characteristics;
- The experimental pressure distribution on the cylinder at different distances from the rotor disk.

6. RESULTS

6.1 Rotor characterization

The aerodynamic behaviour of the helicopter rotor model in hover conditions was characterized by varying the rotor speed and the collective pitch angle in the full operative range. Forces and moments generated by the rotor were measured by means of the six components balance. Particular attention was paid to the thrust (T) and torque (Q) in order to measure the rotor Figure of Merit. The FM is defined as the ratio between the ideal power (P_{ideal}) required to hover, obtained from momentum theory, and the actual power required to hover (P_{meas}) (Leishman [18]). The ideal power is defined as the product between the rotor thrust (T) and the induced velocity (V_i), whereas the real power required is due by the product between the rotor torque (Q) and the rotor speed (ω). Therefore, the Figure of Merit equation is expressed as:

(4) $$FM = \frac{T \cdot V_i}{Q \cdot \omega} = \frac{T\omega R(C_T/2)^{0.5}}{Q \cdot \omega} = \frac{TR(C_T/2)^{0.5}}{Q}$$

where all the variables were measured by the balance (thrust and torque) and by the hale sensor (rotating speed).

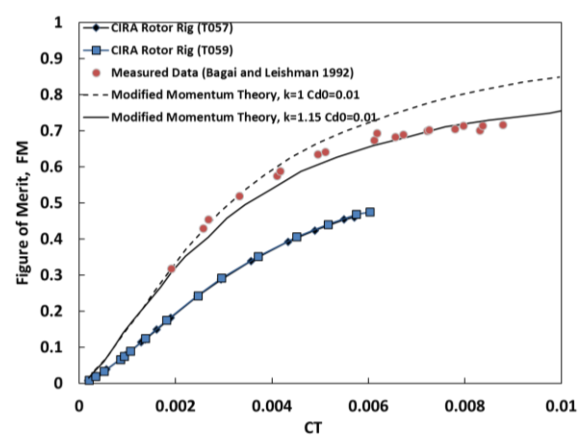

Figure 8: Rotor figure of merit compared with the modified momentum theory discussed in Leishman[18] and the rotor measured data from Bagai and Leishman[19].

The obtained figure of merit, Figure 8, of the model rotor presented a behaviour which was similar to that of a real helicopter as shown in literature (e.g. Bagai and Leishman[19]). The maximum FM, equal to FM=0.48 at CT=0.006, was selected as the rotor testing condition for all the following measures. All test were performed at a rotor thrust of T=12 N and at a rotor speed of ω=1740 rpm, corresponding to a blade tip Reynolds number of 1.47*10^5.

6.2 Rotor Downwash Flow field

The rotor downwash was investigated in terms of ensemble average velocity field. The flow field behaviour was measured in condition of isolated rotor and in presence of the sling load at z=-1R, Z=-2R and z=-2.5R respectively. Only the case with the cylinder at z=-1R and z=-2R are discussed in the following.

For the isolated rotor, the velocity downwash presented three main regions: an external region featured by the wake shear layer; a middle region characterized by the downwash velocity peak at about x=0.8 R; and an inner region distinguished by a smaller vertical velocity due to the presence of the rotor hub and of the fuselage, Figure 9 (upper-left picture). Moving far away from the rotor disk, the viscous diffusion and dissipation phenomena weakened the maximum and minimum peaks of the vertical velocity, approaching a constant value, and increased the shear layer region. The results also showed an asymmetry in the left zone of the rotor wake due to the disturbance generated by the support bar of the model rig.

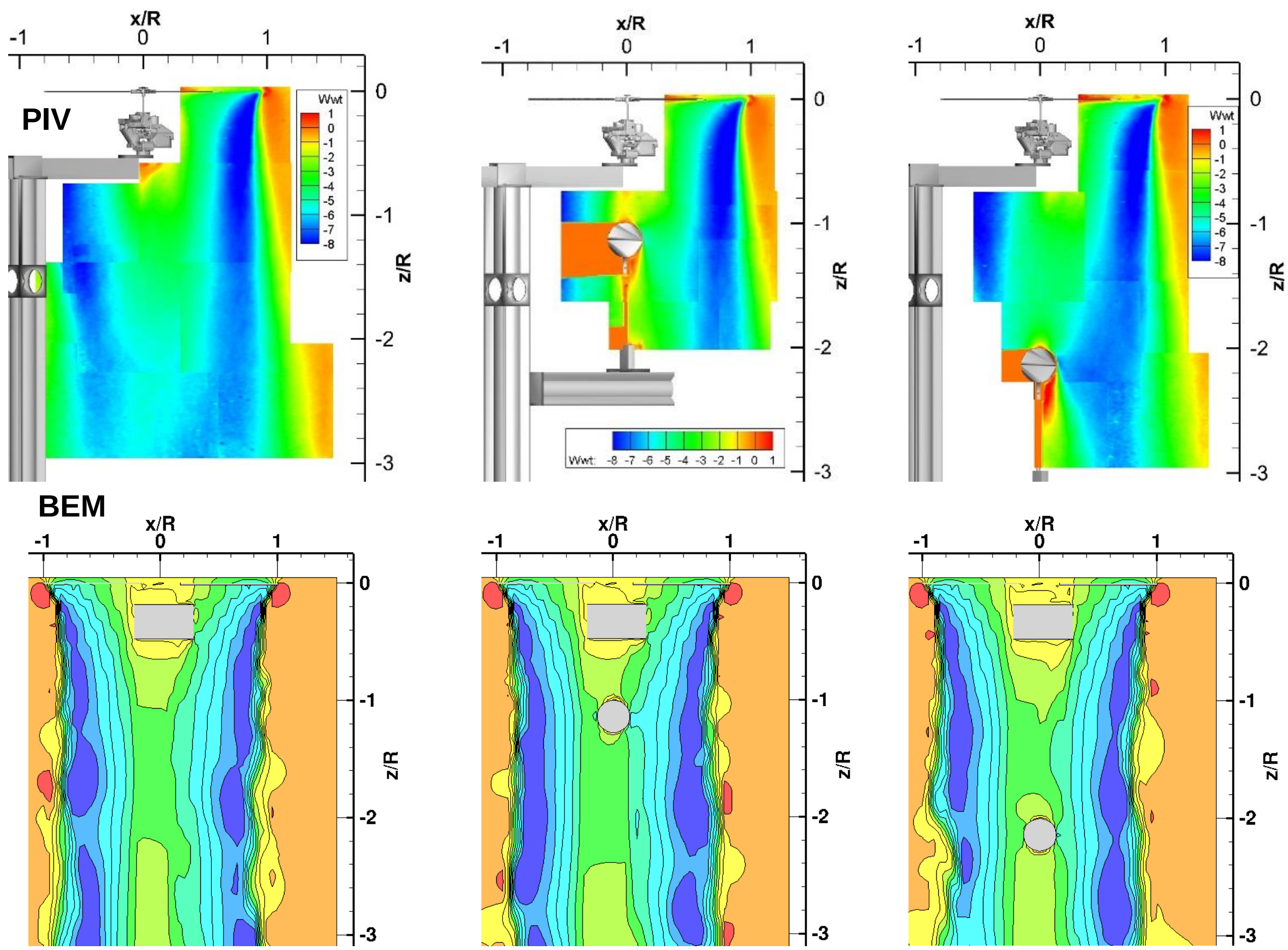

Figure 9: PIV and BEM rotor wake ensemble average velocity field. Vertical component colour maps: rotor in isolation (left), rotor with cylinder in the wake at z= -1R (centre) rotor with cylinder in the wake at z= -2R (right).

The rotor downwash characteristics in the presence of the sling loads were similar to the isolated rotor but with some differences. The presence of the sling load influenced the flow behaviour: contracting the rotor downwash; moving the maximum velocity peak toward the centre of the rotor (x=0.5-0.6 R); and varying the flow conditions in the proximity to the sling loads, Figure 9 (upper-centre and right images).

The presence of the cylinder slightly influenced the rotor downwash in the proximity to the rotor disk, with respect to the rotor in isolation. In the range between z=0 to z=-0.5 R the velocity affected by the presence of the cylinder fully matches the undisturbed downwash, Figure 9 (upper-centre and right diagrams). As the distance from the rotor plane increased, the velocity peak presented a tendency to move closer to the cylinder. For the case of the cylinder located at a distance of z=-1 R beneath the rotor disk, the maximum downwash velocity shifted from x=0.8 R to 0.7 R and the shear layer moved toward the rotor wake centre. The displacement of the downwash peak toward the cylinder was better highlighted by the case of the cylinder at two radii from the disk. The vertical peak velocity was moved toward the new radial position of x=0.5 R instead of 0.8 R. The shift of the maximum downwash produced a contraction of the slipstream as well, Figure 10.

The numerical simulation of the rotor downwash is illustrated in the lower part of Figure 9, for the same experimental test configurations. The comparison with the experiment showed that the numerical shear layer thickness is much thinner, with resulting higher velocity gradients and mostly constant in the downstream direction. This was mainly explained by the absence of a dissipation scheme in the wake modelling. The predicted intensity of the tip vortex roll-up was stronger and influenced a larger outward region in the radial direction. The presence of the cylinder accelerated the flow in the proximity to its surface as was observed in both the experiment and in the numerical solution. Nevertheless, the potential nature of the flow solver was unable to detect the recirculation downstream of the cylinder, which was instead observed in the measurements. The asymmetry in the fuselage geometry and its set-up with respect to the rotor hub produced asymmetries in the downwash.

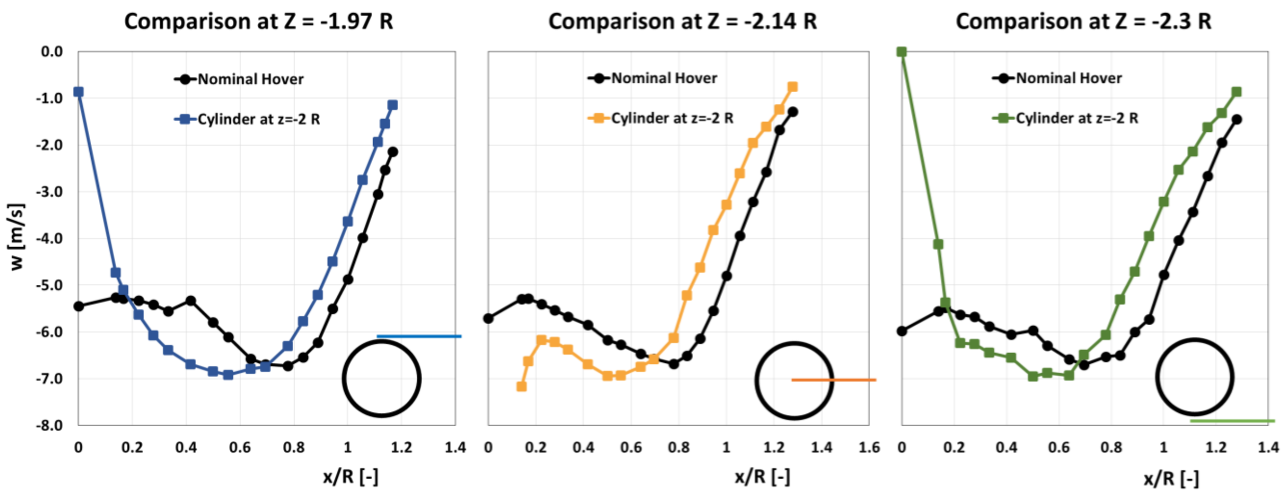

Figure 10: Vertical velocity comparison between isolated rotor and with cylinder at distance of z=-2R. The velocity behaviour along radial axes at z=-1.94R, z=-2.14R and z=-2.3 R are shown from the left to the right, respectively.

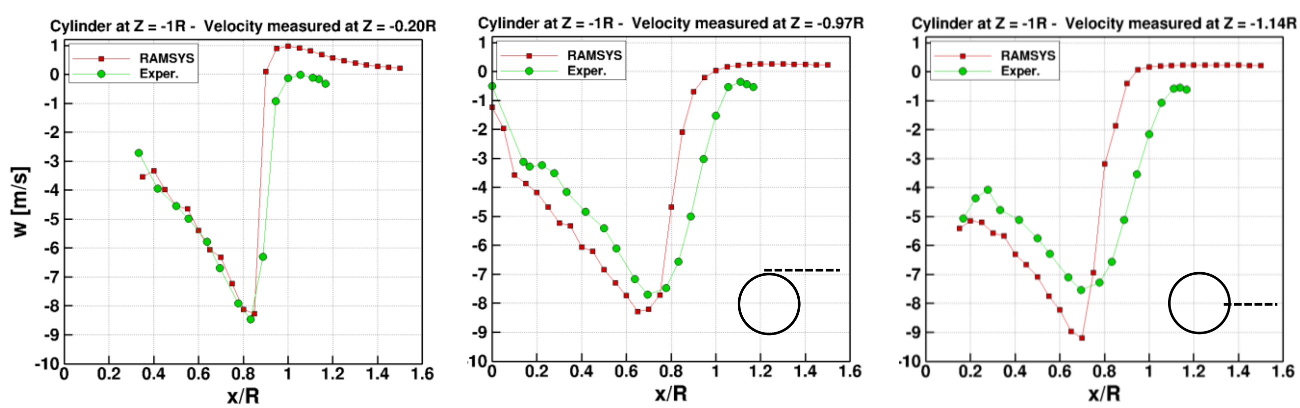

Figure 11: PIV vs numerical vertical velocity comparison with cylinder at a distance of z = -1R.

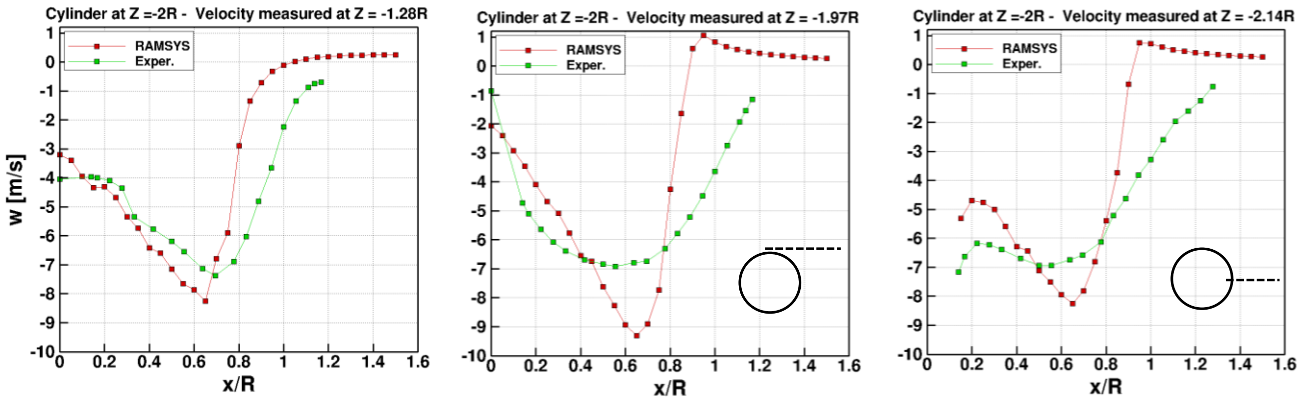

Figure 12: PIV vs numerical vertical velocity comparison with cylinder at a distance of z = -2R.

Figure 11 and Figure 12 provided more details about the differences between the numerical-experimental comparisons in terms of the time-averaged vertical velocities. They were evaluated at selected distances downstream of the rotor, for the cylinder position 1R and 2R below the disk, respectively. In particular, in the immediate proximity to the blades, the agreement with the experiment was extremely satisfactorily inside the rotor wake, whereas outside the shear layer the influence of a stronger tip vortex roll-up was observed, Figure 11 left. In the region around the cylinder location, the measurements highlighted the combined viscous effects of diffusion and dissipation, which produced a thickening of the measured shear layer and a reduction in the peak velocity, particularly when the cylinder was located at 2R, thus indicating that, for the Reynolds number of the investigated test, the structure of the real wake started losing its coherence at 2 rotor radii below the blades. These viscous effects were not fully captured by the wake model used for the numerical simulations. The acceleration induced by the cylinder was clearly detected, around x/R = 0.2, in Figure 11 right and Figure 12 right, in both the numerical and experimental results, despite some quantitative differences were observed.

6.3 Tip Vortices

Dedicated PIV measurements were carried out with a finer spatial resolution in order to investigate the tip vortices in the region enclosed from the rotor disk to the distance of 1 radius downward. The ensemble averaged velocity field showed the shear layer region surrounding the rotor downwash wake, Figure 13 (left image). Similar results were obtained by the numerical mean velocity field, Figure 13 (right image) except for some differences. The PIV velocity magnitude presented the shear layer origin located at about x/R= 0.96 due to the blade deflection, a marked increment of the shear layer moving downward from the rotor disk due to the diffusion and a reduction of the vertical velocity already visible at around z/R=-0.7 due to the dissipation effect. Instead, the numerical results located the origin of the shear layer at x/R=1, having imposed rigid rotor blades. In addition, moving down from the rotor the shear layer increment and the velocity dissipation were negligible with respect to the PIV data.

The PIV and BEM instantaneous velocity fields clearly showed the presence of several tip vortices in the proximity to the blade, Figure 14. The PIV measurements were not phase locked with the rotor so that the age of the vortices was estimated on the base of the position of the tip vortices with respect to the tip blade. The PIV tip vortices presented larger dimensions and were in smaller number, three instead of four, with respect the BEM velocity field. The vortex trajectory were similar except for the youngest tip vortices that in case of PIV measurement were released by the deflected blade at about x/R=0.96.

A preliminary analysis of the tip vortices was performed on the full set of PIV instantaneous vorticity maps with the aim to detect the vortex centres and to measure the main characteristics. As a first attempt, the centre of the vortices was identified as the maximum of the out of plane vorticity ω_y (Vollmers[20]). Once the centre was detected, the tangential velocity and the vorticity intensity versus the vortex radius was calculated. The results, shown in Figure 15 and Figure 16, provided the radius of the vortex core, the tangential velocity and the maximum of the vorticity for the BEM tip vortices at age of ψ = 10° and the closest PIV tip vortex selected by the analysis of more than 300 velocity fields. The characterization of the tip vortex indicated that, with respect to the BEM results, the PIV measurements provided, for the majority of the cases, a higher value of the vorticity magnitude, of the tangential velocity (V_θ), and a larger vortex core radius (r_c).

The distribution of the vortex centres showed the highest concentration in the proximity to the rotor disk and that their location was enclosed in the shear layer region, Figure 17. Moving downward the data scattering increased, distributing the centres of the vortical structures both outside and inside the ensemble averaged downwash. The maximum vorticity peaks showed a reduction moving away from the rotor disk despite the highly dispersed data, Figure 18. The calculated weighted average function indicated a constant negative slope $\delta(\omega_y c)/V_{tip})/\delta(z/R)$ =-7 in the region from z=-0.1R to z=-0.8R, followed by a slope reduction in the proximity to z=-1R equal to $\delta(\omega_y)/\delta(z) = -1.5$.

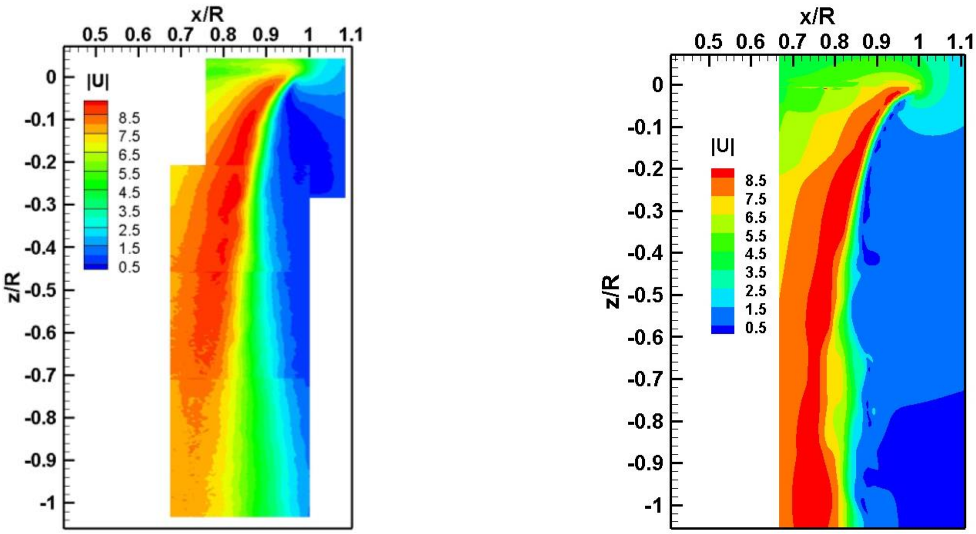

Figure 13: PIV (left) and numerical (right) ensemble average velocity magnitude colour map.

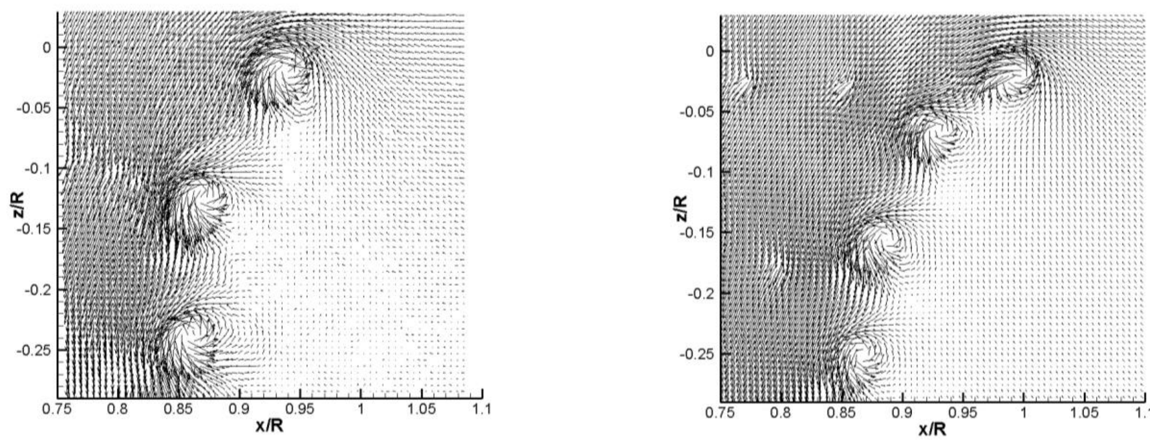

Figure 14: Comparison between PIV (left) and numerical (right) tip vortex locations

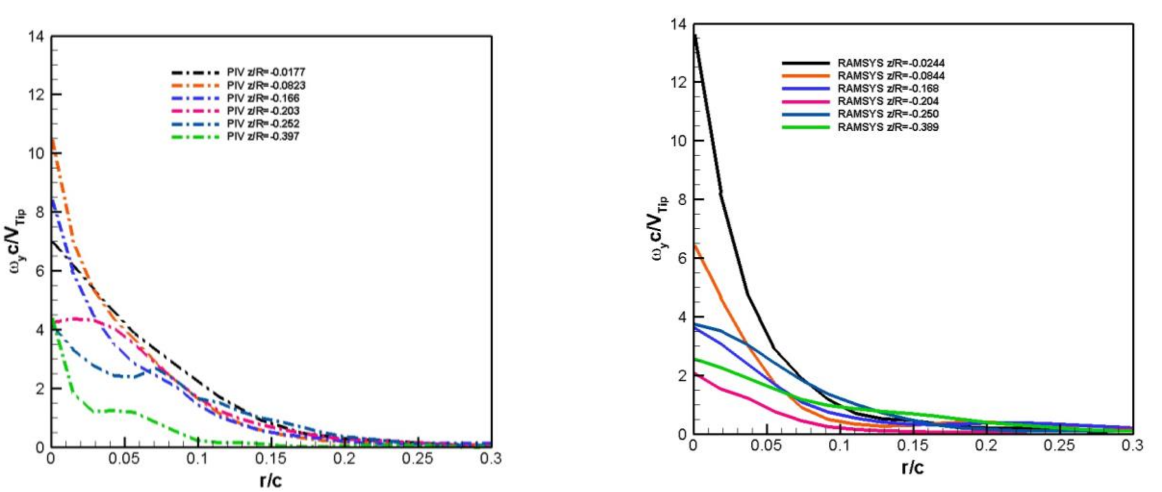

Figure 15: PIV and RAMSYS normalised out of plane vorticity vs vortex radius

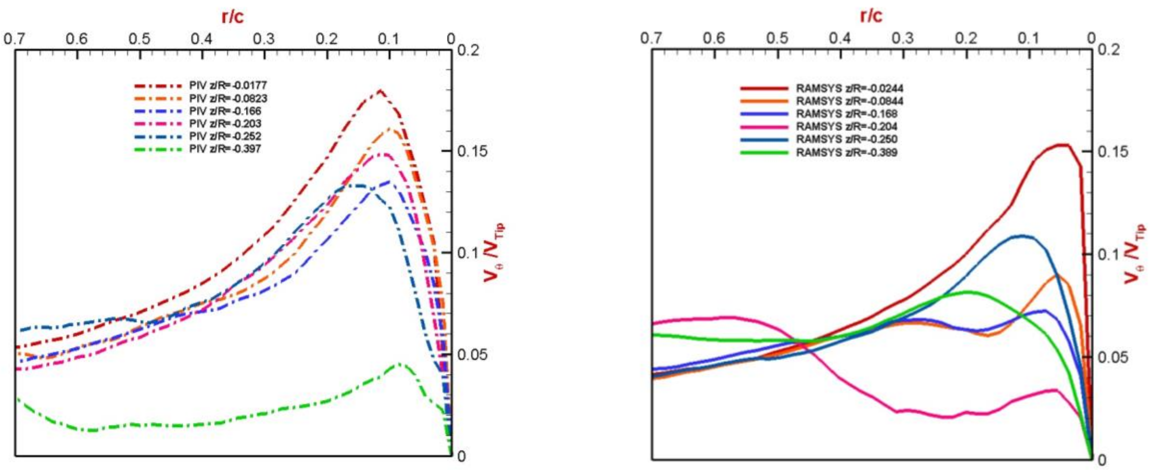

Figure 16: PIV and RAMSYS normalised tangential velocity vs vortex radius

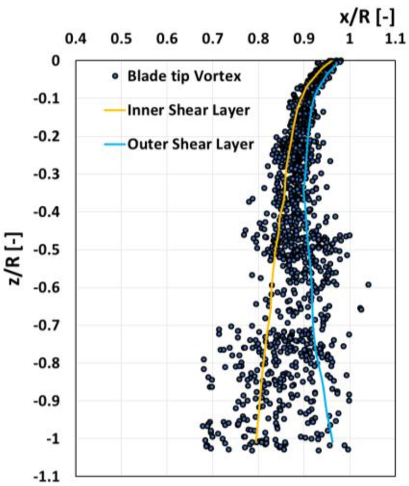

Figure 17: PIV tip vortices location together with the inner and outer shear layer of the main rotor downwash.

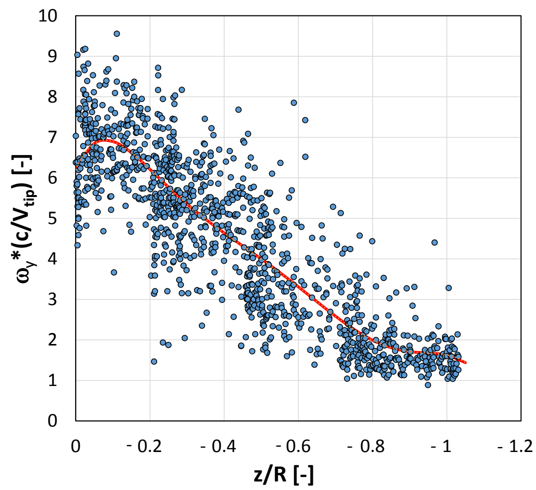

Figure 18: PIV tip vortex vorticity distribution vs the distance from the rotor plane. A weighted average is plotted (red line).

6.4 Cylinder pressure distribution

The radial pressure distribution presented a similar trend for all the positions of the cylinder, Figure 19. The pressure maximum value was located in the proximity to the stagnation point on the top surface of the cylinder, for then decreasing in correspondance with the flow acceleration up to a minimum at cylinder azimuth angle of about $\pm 80°$ followed by a pressure increment up to the occurring of the flow separation.

The spanwise pressure distribution showed a symmetric parabolic behaviour, with the origin located in the cylinder centre, for the closest cylinder location to the rotor disc (z=-1R). The other two positions had a mainly a linear behaviour with higher values on the left of the rotor wake due to the asymmetry induced by the support bar, Figure 20.

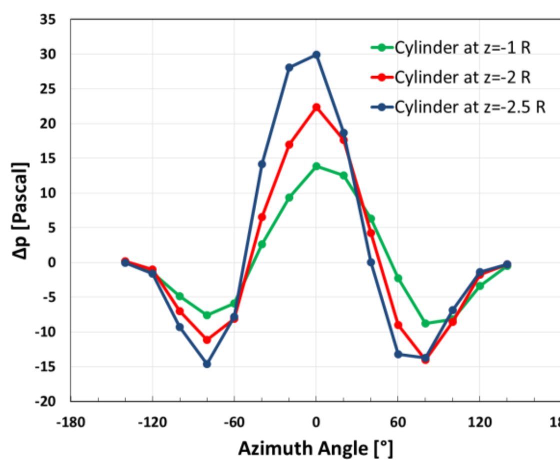

Figure 19: Pressure distribution on the symmetry plane of the cylinder varying the distance from the rotor disk.

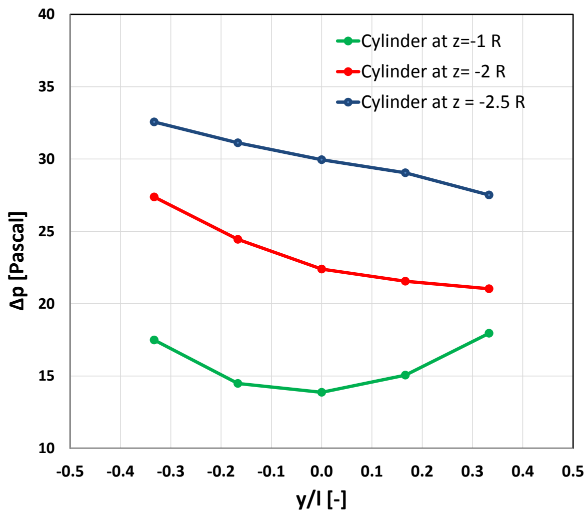

Figure 20: Pressure distribution on the spanwise of the cylinder varying the distance from the rotor disk.

The cylinder pressure distribution confirmed the rotor downwash results, showing, in particular, that the closest distance to the rotor disk (z=-1R) produced the smallest induced loads being in the wake region interested by the rotor hub and fuselage. Moving downward, the diffusion effect increased the downwash speed and consequently the pressure loads

An asymmetry in the wake was also detected by the pressure behaviour as encountered in the wake downwash investigation.

7. CONCLUSIONS

An experimental test campaign was carried out on a four-blade rotor rig in order to investigate the downwash effect on a sling load located beneath the helicopter fuselage. In particular, the aim was to investigate the loads induced by the rotor wake on an experimental RLV model during the initial phase of a drop tests.

To do this, the rotor wake characteristics were measured in hover condition with and without the presence of the sling load. The effect of the rotor wake on the immersed body was considered at different distances from the rotor disk by measuring the induced surface pressure distribution. The wake and body mutual interference was investigated measuring the velocity flow field through two components planar PIV. A circular cylinder was selected being representative of a typical sling load and for the simplicity of the geometry for numerical simulations.

The rotor rig figure of merit was measured by varying the operative conditions in terms of rotating speed and collective angle. The full downwash wake was measured up to a distance of z=-3R from the rotor disk. The presence of the cylinder induced a shrinkage of the wake by shifting the position of the maximum velocity peak toward the centre of the wake. For the case of the cylinder at z=-2R the rotor downwash peak shifted until touching the cylinder.

At the investigated Reynolds number, starting from 2R downstream the rotor disk, a significant thickening of the measured shear layer and a reduction in the peak velocity was observed due to the combined diffusion and dissipation viscous effects.

The rotor blade tip vortices were investigated with a finer spatial resolution. Main vortex characteristics in terms of vorticity, tangential velocity and core radius were measured. A vorticity dissipation trend with the distance from the rotor disk resulted in two regions characterised by different slopes.

The measured pressure distribution on the sling load surface presented the lowest increment for the cylinder located at 1 radius below the disk and the highest increment for the cylinder at 2.5 R due to the diffusion effects.

Preliminary numerical investigations were carried out for the same experimental test configuration in terms of the rotor downwash, swirl velocity and vorticity. The comparison with the measurements showed a satisfactory agreement of the ensemble averaged velocity field in the proximity to the rotor disk, whereas some discrepancies, mainly caused by the absence of a dissipative scheme in the wake modelling, occurred farther downstream where the viscous effect played a stronger influence (≥ 1R). For these reasons, the simulated shear layer turned out to be thinner, and the velocity peak in the downwash was higher than the PIV one.

Future development will be addressed to:

- The implementation of more robust methods for the detection of the vortex centre and their characterization;
- The evaluation of pressure force on the sling load;
- The numerical tip vortex location at different vortex ages;
- The implementation of a wake dissipation model;
- The numerical estimation of the sling load pressures.

8. ACKNOWLEDGMENTS

The authors would like to acknowledge the student Manuela Coletta for the valuable support provided during the tip vortex characterization.

9. REFERENCES

[1] Gabel, R., Wilson, J.G., (1968) Test Approaches to External Sling Load Instabilities, Journal of the American Helicopter Society, Vol.13 Nr.3, July;

[2] Rajagopalan R. G., (2000) A Procedure for Rotor Performance Flowfield and Interference: A Perspective. doi:10.2514/6.2000-116;

[3] Parsch A., (2005-2009) Directory of U.S. Military Rockets and Missiles Appendix 4: Undesignated Vehicles X-37/X-

40,http://www.designation-systems.net/dusrm/app4/x-37.html;

[4] Janovsky R., Behr R., (2005) Flight Testing and Test Instrumentation of PHOENIX, proceedings of the Fifth European Symposium on Aerothermodynamics for Space Vehicles (ESA SP-563), Cologne, Germany, Nov. 8-11, 2005;

[5] Rufolo G. C., Gallego Sanz J. M., Valenzano G., Marino G., Guidotti G., Vernillo P., (2013) ESA Intermediate Experimental Vehicle System Synthesis Test. Design, Verification and Implementation," presented at the 64rd International Astronautical Congress, Beijing, China;

[6] Foust, J., (2017) Sierra Nevada satisfied with Dream Chaser glide test, SpaceNews. http://spacenews.com/sierra-nevada-satisfied-with-dream-chaser-glide-test/;

[7] Visingardi A., De Gregorio F., Schwarz T., Schmid M. et al, (2017) Forces on Obstacles in Rotor Wake – A GARTEUR Action Group, 43rd European Rotorcraft Forum proceedings, Milan, Italy, September 12-15;

[8] Prosser D.T. and Smith M.J., (2014) Three-dimensional bluff body aerodynamics and its importance for helicopter sling loads. 40th European Rotorcraft Forum proceedings, Southampton, UK, September 2-5;

[9] Zdravkovich M.M. (1997) Flow Around Circular Cylinders. Fundamentals, vol.1, chapter 6. Oxford University Press;

[10] Catalano P, Wang M., Iaccarino G., Moin P. (2003) Numerical Simulation of the Flow around a Circular Cylinder at High Reynolds Numbers. International Journal of Heat and Fluid Flow, vol.24, pp. 463—469;

[11] Hart DP (2000). Super-resolution PIV by recursive local-correlation. Journal of Visualization, 3(2), 187–194. doi:10.1007/BF03182411;

[12] Raffel M.,Willert C. E.,Wereley S. T., and Kompenhans J., (2007) Particle Image Velocimetry - A Practical Guide, Springer-Verlag Berlin Heidelberg, 2nd edition. doi: 10.1007/978-3-540-72308-0.

[13] Martin P.B., Pugliese G.J., Leishman J.G., Anderson S.L., "Stereo PIV measurement in the wake of a hovering rotor," presented at the 56th AHS Annual Forum, Virginia Beach, VA, USA, 2000;

[14] Visingardi, A., D'Alascio, A., Pagano, A., Renzoni, P., "Validation of CIRA's Rotorcraft Aerodynamic Modelling SYStem with DNW Experimental Data," 22nd European Rotorcraft Forum, Brighton, UK, Sept. 1996;

[15] Scully, M.P., "Computation of Helicopter Rotor Wake Geometry and Its Influence on Rotor Harmonic Airloads," MIT Aeroelastic and Structures Research Laboratory, ASRL TR 178-1, March 1975;

[16] Squire, H.B., "The Growth of a Vortex in Turbulent Flow," The Aeronautical Quarterly, 16: p. 302-306, August 1965;

[17] Baghwat, M.J., Leishman J.G., "Generalized Viscous Vortex Model for Application to Free-Vortex Wake and Aeroacoustic Calculations," presented at the 58th AHS Annual Forum, Montreal, Canada, June 2002;

[18] Leishman J.G., (2000) Principles of Helicopter Aerodynamics. Cambridge University Press, pag.71;

[19] Bagai A. and Leishman, J. G., (1992) Experimental Study of Rotor Wake/Body Interactions in Hover. Journal of the American Helicopter Society, Volume 37, Number 4, 1 October 1992, pp. 48-57(10);

[20] Vollmers H., (2001) Detection of vortices and quantitative evaluation of their main parameters from experimental velocity data. Meas Sci Technol 12:1199-1207.